Radon Transform Methods and Their Applications in Mapping Mantle Reflectivity Structure

Yu Jeffrey Gu · Mauricio Sacchi

Abstract   This paper reviews the fundamentals of Radon-based methods using examples from global seismic applications. By exploiting the move-out or curvature of signal of interest, Least-squares and High-resolution Radon transform methods can effectively eliminate random or correlated noise, enhance signal clarity, and simultaneously constrain travel time and ray angles. The inverse formulation of the Radon transform has the added benefits of phase isolation and spatial interpolation during data reconstruction. This study presents a 'cookbook' for Radon-based methods in analyzing shear wave bottom-side reflections from mantle interfaces, also know as *SS* precursors. We demonstrate that accurate and flexible joint Radon- and frequency-domain approaches are particularly effective in resolving the presence and depth of known and postulated mantle reflectors.

Keywords   Radon transform · SS precursor · Seismic discontinuities ·
Plumes · Hotspot · Mantle structure · Phase transition · Lower mantle reflectors ·
Subduction zone

1 Introduction

Attenuation of unwanted events such as surface waves and multiples (Yilmaz 1987) poses a key problem in exploration seismic data processing. Effective solutions to this problem often exploit the move-out or curvature differences between offending events and the event of interest. One such solution is the Radon transform, an integral transform (Radon 1917) that was later adapted not only for the removal of multiple reflections (Thorson and Claerbout 1985; Hampson 1986; Beylkin 1987; Sacchi and Ulrych 1995), but also for wide-ranging applications in astrophysics (Bracewell 1956), computer tomography (Cormack 1963) and more recently, regional and global seismology (Gorman and Clowes 1999; Wilson and Guitton 2007; Ma et al. 2007; An et al. 2007; Gu et al. 2009). Radon transforms in their discrete form are known for different variations (linear, parabolic, hyperbolic, generalized)

Y. J. Gu (✉) · M. Sacchi
Department of Physics, University of Alberta, Edmonton T6G2G7, Canada
e-mail: jgu@phys.ualberta.ca

and names (slant stack, beam-forming, fan filtration, $\tau-p$ transform). The method of choice in a specific application depends on the nature of the source excitation, the inherent properties of the target signal and, in some cases, computational cost (e.g., Kappus et al. 1990). For example, parabolic and hyperbolic transforms are the preferred Radon methods if the data after move-out correction are best characterized by a superposition of parabolas and hyperbolas, respectively. Inverse formulations have also been developed to enhance the flexibility and resolution of Radon solutions. In the cases of parabolic (Sacchi and Ulrych 1995) and hyperbolic (Thorson and Claerbout 1985) Radon transforms, the operator capable of inverting the Radon transform is designed in ways that, when properly executed, the data in the Radon domain exhibit minimum entropy or maximum sparseness (synonymously used in this study to describe a distribution of isolated signals in the Radon domain).

The success of Radon-based methods in exploration seismology can potentially be replicated in global seismic surveys of the crust and mantle reflectivity structure. Apart from the obvious scale difference between exploration (<20 km) and global (typically >100 km) problems, key objectives such as signal isolation and enhancement, noise reduction, and data reconstruction are nearly independent of the applications. Furthermore, in properly designed global problems, the nominal resolution estimated from the ratio between wavelength (tens to hundreds of kilometers) and target dimension (often, continent-scale) could rival the average resolution of exploration imaging. For instance, recent high-resolution images of the Japan slab (a strong dipping reflector) based on array analyses of earthquake data (Kawakatsu and Watada 2007; Tonegawa et al. 2008) draw many parallels to earlier sections of back-scattered head waves (Clayton and McMechan 1981) and present-day reflection profiles of salt domes in oil/gas surveys. Similar success has been documented at other geographical locations and depths using array methods (see Rost and Thomas 2002; also see papers in this Special Issue). Coordinated efforts and substantial resources similar to those put forth by the ongoing USArray project have now enabled the 'global community' to take full advantage of various array methods that predicate on superior data density and distribution.

In this article we discuss the problem of designing a Radon operator, one of the many original contributions of exploration seismology, to isolate and filter plane waves reflected from mantle rocks. The solution entails a transformation that, in the absence of filtering in the transform domain, is capable of recovering the original data. Our selected case studies of low-amplitude, underside reflections (or, *SS* precursors; Fig. 1a) aim to accentuate the great potential of Radon-based techniques in resolving the large-scale seismic structure, dynamics and, possibly, mineralogy within the Earth's mantle.

2 Theory

The section reviews the fundamentals of Radon Transform (RT) methods. While advanced RT methods have distinct advantages over classical RT approaches, they are based upon the same elementary operations such as *Delay-and-Sum* and *Slowness Slant Stacking*. For completeness and continuity we summarize the basic formulations and global seismic applications of each approach. We mainly emphasize the role of Radon transform as a signal identification and enhancement tool, a view often shared in exploration seismic applications. It should be recognized, however, that Radon transforms can be generalized to solve the linear Born scattering problem with asymptotic Green functions. We defer the discussion of Generalized Radon Transform (GRT) method and its contributions to

Fig. 1 **a** Schematic ray diagram for *SS* and *SdS* (d represents an mantle interface at d-km depth). The actual depth of the interface could differ (see illustration). The *star* denotes an earthquake location. **b** Signal enhancement using the Delay-and-sum approach. The example is modified from Fig. 5 of Gu and Dziewonski (2002) based on correlations computed relative to *S660S*. The *S410S* signal is significantly enhanced by averaging the individual correlations with the *SS* pulse
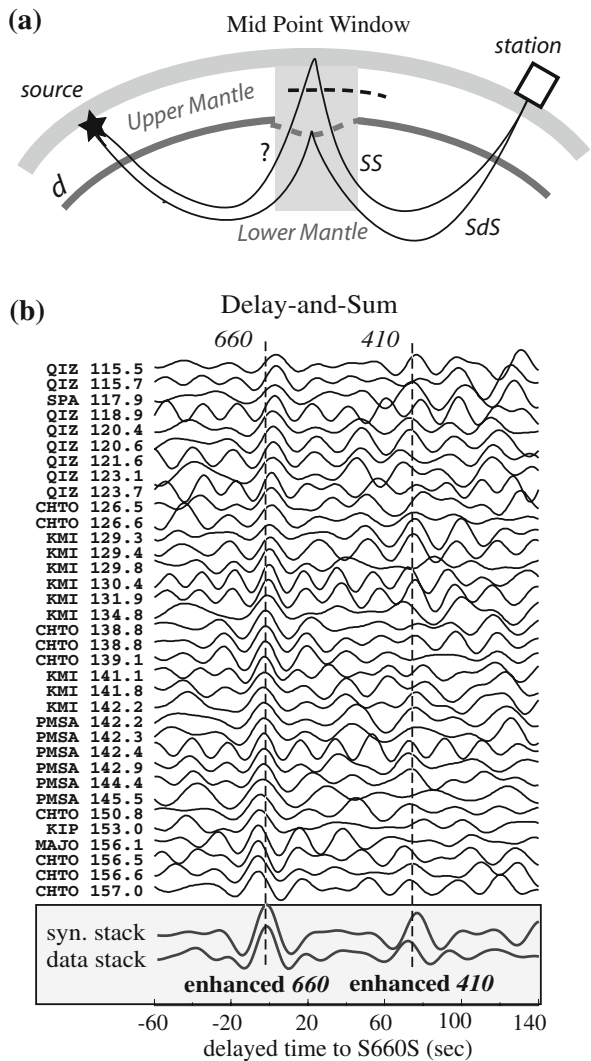
applications in exploration (Beylkin 1985; Miller et al. 1987) and deep-Earth (Wang et al. 2006) seismology to the original studies.

2.1 Delay-and-Sum

Observations of minor crust and mantle interfaces can be challenging due to low impedance contrasts. For example, the amplitude of a typical precursory arrival is 4–8% of the size of the surface reflection *SS* (Fig. 1b; e.g., PREM; Dziewonski and Anderson 1981), which is barely within the detection threshold of conventional processing techniques. A reliable assessment of the signals from individual records in the presence of comparable noise levels is impractical if not impossible. A simple remedy is to compute the weighted

average of time-domain records with similar properties (e.g., records from a common shot or mid-point gather) while assuming the noise distribution is approximately Gaussian (e.g., Shearer 1991, 1993; Gu et al. 1998; Flanagan and Shearer 1998; Deuss and Woodhouse 2002). The time-domain delay-and-sum (also known as *stacking*) procedure can be expressed as

$$d(t) = \frac{1}{N} \sum_{i=1}^{N} w_i d_i(t - t_0) \tag{1}$$

where $d(t)$ represents the weighted average of seismic traces d_i at a delay $t - t_o$ from a reference time t_o. This procedure can improve the SNR by a factor of $\sqrt{N}$, where N is the total number of seismograms in the averaging process (e.g., Shearer 1991). Further SNR enhancement may be possible by assigning non-uniform weights according to the SNR of the respective records (e.g., Shearer 1993; Gu et al. 1998). Figure 1b shows an array of delayed long-period records before and after stacking (Gu and Dziewonski 2002). The vastly improved clarity of *S410S* after delay-and-sum operation enables accurate measurements of the signal's arrival time and amplitude. We refer the reader to Deuss (this issue) for more detailed discussion of the global applications and error estimates of this time-domain approach.

2.2 Slowness Slant Stack (Vespagram)

The standard delay-and-sum approach is most effective when: (1) the noise spectrum within the phase window of interest is 'white', and (2) the chosen slowness in computing the delay times is accurate. In practical applications, however, phase identification and time/amplitude determination are often complicated by the presence of strong correlated noise and/or offending seismic arrivals. An obvious improvement over the aforementioned time-domain approach is to construct slowness slant stacks, a variation of the "vespa" process (Davies et al. 1971; Rost and Thomas 2002) that simultaneously constrain the timing and slowness of a seismic arrival. Using similar notations as Eq. 1, the summation can be written as

$$D_j(t) = \frac{1}{N} \sum_{i=1}^{N} w_i d_i(t + \delta t_{ij}(\Delta)), \quad \text{where } \delta t_{ij}(\Delta) = s_j(\Delta_i - \Delta_0) \tag{2}$$

In this equation, $\delta t_{ij}(\Delta)$ represents the time shift to the i-th seismogram according to the j-th slowness (s_j) for a source-receiver pair separated by distance Δ. The scalar weight w_i is used to assign a measure of quality to the j-th seismogram in the summation (or stacking) of all traces via the delay-and-sum approach. This procedure marks a simple transformation from time–distance domain to Radon ($\tau - p$) domain, assuming that a properly chosen slowness s (or ray parameter p) leads to enhanced focusing of the seismic energy from a desired arrival (Fig. 2). The existence, depth, and reflectivity of a target seismic structure can then be readily inferred from the difference between empirically determined slowness and the reference/expected value for the seismic phase in question. Variations to this beam-forming procedure (e.g., Kruger et al. 1993) have been introduced to simultaneously determine time, slowness and azimuth variations (see review of the 'vespa' process, Rost and Thomas 2002).

The slant stacking method defined by Eq. 2 has wide-ranging global seismic applications owing, in large part, to its simplicity. It is instrumental to the success of mantle

Fig. 2 *Schematic diagram* showing the forward Radon procedure. Stacking along the ray parameter *p* maps the time-domain peaks into a strong energy focus in the Radon domain (*dark solid circle*). Conversely, stacking along a ray parameter *p2* leads to negligible Radon energy due to major mismatches with the travel–time slope of the major arrivals
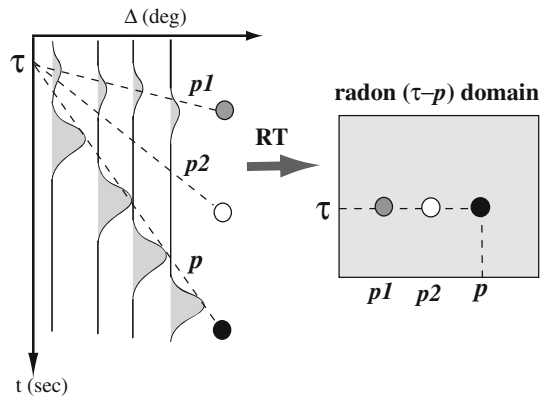
reflectivity imaging based on careful analyses of $P'P'$ precursors (Vidale and Benz 1992), *PP* precursors (Estabrook and Kind 1996), P-to-S converted waves (Niu and Kawakatsu 1995, 1997) and *SS* precursors (Gossler and Kind 1996; Gu et al. 1998). The availability of regional (e.g., in California and Japan) and global (GSN) seismic arrays provides the necessary frequency and spatial resolutions for these endeavors. For example, the analysis with the slowness stack method of *SS* precursors (Fig. 3) shows robust Radon amplitudes caused by well-known (e.g., the 410 and 660 km) and postulated (e.g., 520 km and lithospheric) mantle discontinuities or reflectors. The averaging radii are of continent-scale and the observed reflectivity structure accounts for all source-receiver azimuths beneath the study region.

2.3 Generic Transformation Methods

The slant stacking approach outlined above exemplifies a class of transformation methods that maps the seismic data to a surrogate domain where individual signals (waveforms) could be easily isolated, classified, filtered and enhanced. The framework of a generic transformation method is illustrated using a simple cartoon (Fig. 4). Suppose the data *d* is composed of the superposition of four "waveforms" represented by d_i ($i = 1,\ldots, 4$) where

$$d = d_1 + d_2 + d_3 + d_4, \tag{3}$$

then a linear transformation that maps the data *d* into *m* in the new domain becomes

$$m = m_1 + m_2 + m_3 + m_4. \tag{4}$$

We have assumed the integrity of the each waveform is preserved in the transform domain, that is, d_i maps to m_i through a proper transformation. The forward transformation from time–distance domain to reduced time-slowness domain not only overcomes travel time complexities (e.g., triplication) caused by heterogeneous structures (e.g., Shearer 1999; Chapman 2004), but also enables filtration or enhancement of m_i in the transformed domain. In other words, the resulting event d_i after the inverse transformation can be sufficiently isolated from signal *d* in the original domain (see Fig. 4). This simple concept paves the way for the Radon transform methods examined below.
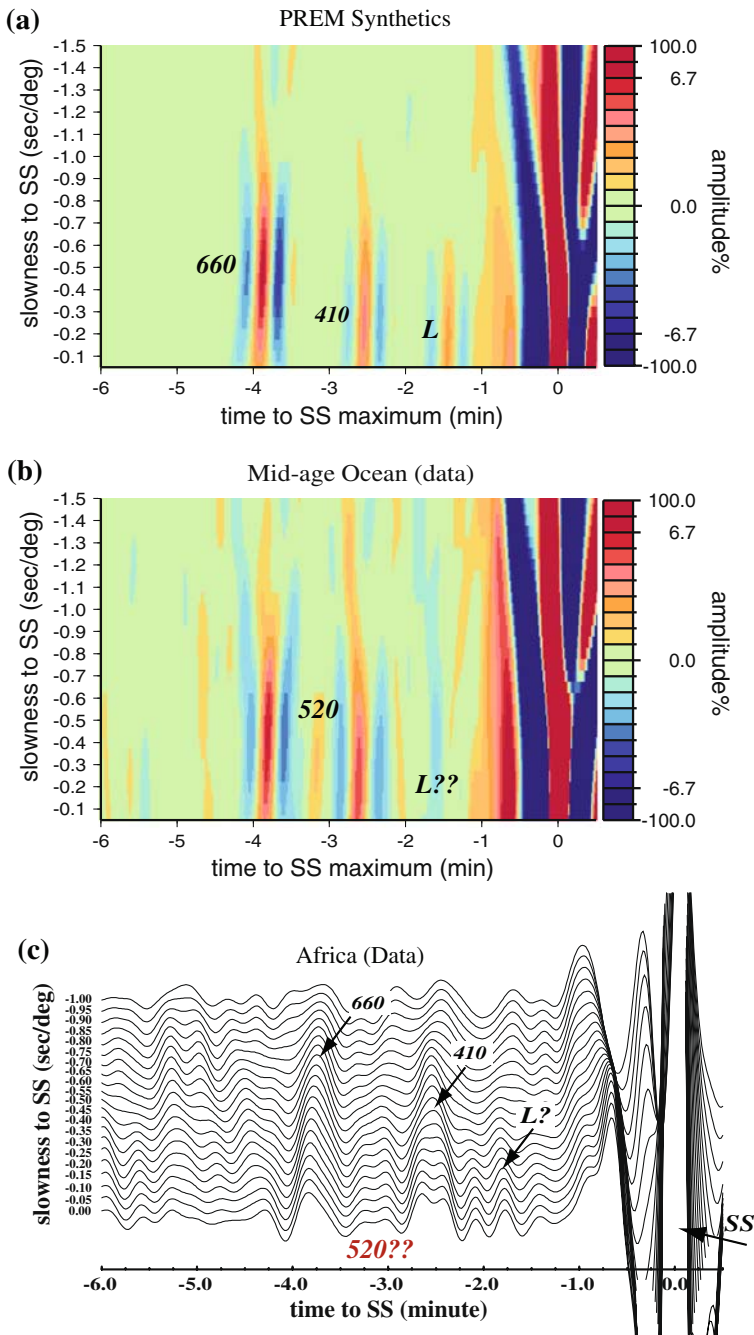
Fig. 3 Slowness slant stacks of *SS* precursors. The figure combines results from Fig. 3 of Gu et al. (1998) and Fig. 4 of Gu et al. (2001). PREM synthetic seismograms contain clear *L* (lithspheric discontinuity), *S410S* and *S660S* signals, but the *L* reflection is missing beneath Africa while *S520S* (not predicted by PREM) is present under global oceans. The resolution in slowness is low in all three examples

Fig. 4 A *flow chart* showing the process of Radon-based inversion and signal isolation. The transformation enables the extraction of Radon signal (m_1) and the corresponding seismic arrival (d_1)
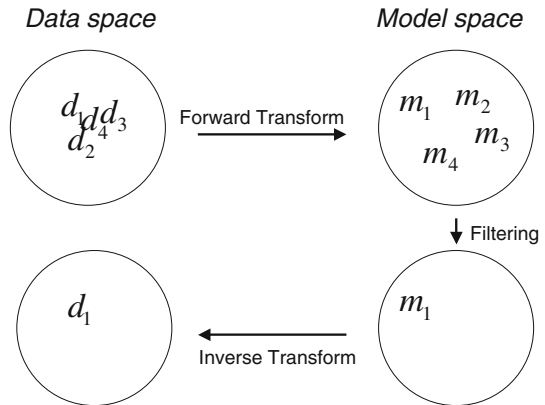
2.4 Radon Transform Methods

Combining notations from Eqs. 2–4, Radon transform can be expressed by the following operator that is, in essence, the integration of the data along a given travel–time curve

$$m(\tau, p) = \sum_{i=1}^{N} d(t = \phi(\tau, \Delta, p), \Delta_i) \qquad (5)$$

for some function ϕ that depends on reduced time τ, epicentral distance Δ and ray parameter p. One can select one of the following integration paths for the applications:

$$
\begin{aligned}
\phi(\tau, \Delta, p) &= \tau + p\Delta & \text{Linear Radon Transfrom} \\
\phi(\tau, \Delta, p) &= \tau + p\Delta^2 & \text{Parabolic Radon Transfrom} \\
\phi(\tau, \Delta, p) &= \sqrt{\tau^2 + p\Delta^2} & \text{Hyperbolic Radon Transfrom.}
\end{aligned}
\qquad (6)
$$

All three transform methods require a summation along tentative ray-parameters and place the resulting sum at a point (τ, p), despite different assumptions about the distance–time relationships exhibited by the signal of interest in the untransformed domain. Linear and parabolic Radon transforms are most pertinent to the analysis of *SS* precursors (see Sect. 4), while hyperbolic Radon transform is more suitable for discriminating primary reflections from multiples (Hampson 1986; Sacchi and Ulrych 1995; Trad et al. 2002).

   Equation 6 represents a simple mapping from data space to the transform domain but, for the purpose of data reconstruction, it is often more useful to define the Radon transform via an inverse formulation

$$d(t, \Delta) = \sum_{p} m(\tau = \phi'(t, \Delta, p), p) \qquad (7)$$

where, for the linear Radon Transform, the integration path is given by

$$\phi'(t, \Delta, p) = t - p\Delta \qquad (8)$$

Equation 8 now consists of an expression that transforms a point in (τ, p) into a linear event (t, Δ). The main advantage is that the Radon transform $m(\tau, p)$ is now obtained by solving

a linear inverse problem of the form $d=Am$, where A is the sensitivity matrix and the d is the data vector.

2.5 Inversion of Radon Transform

Details pertaining to the synthesis of Eq. 8 were provided by Thorson and Claerbout (1985) and Hampson (1986). In this review we mainly focus on a frequency-domain solution adopted by An et al. (2007). By Fourier transform both sides of Eq. 8 and subsequently apply the Fourier delay theorem (Papoulis 1962), we obtain the following expression for each angular frequency ω:

$$D(\omega, \Delta_k) = \sum_{j=1}^{NP} M(\omega, p_j) e^{-i\omega \Delta_k p_j}, \quad k = 1, \ldots, N \tag{9}$$

where N is the total number of time series in the data gather, ω is a single angular frequency and NP denotes the total number of ray parameters within the desired $\tau-p$ range. Capitalized letters D and M represent the Fourier transform of d and m (see Eq. 7), respectively. Equation 9 represents a matrix equation of the form

$$\begin{pmatrix} D(\omega, \Delta_1) \\ D(\omega, \Delta_2) \\ . \\ . \\ . \\ D(\omega, \Delta_N) \end{pmatrix} = \begin{pmatrix} e^{-i\omega\Delta_1 p_1} & e^{-i\omega\Delta_1 p_2} & . & e^{-i\omega\Delta_1 p_M} \\ e^{-i\omega\Delta_2 p_1} & e^{-i\omega\Delta_2 p_2} & . & e^{-i\omega\Delta_2 p_M} \\ . & . & . & . \\ . & . & . & . \\ . & . & . & . \\ e^{-i\omega\Delta_N p_1} & e^{-i\omega\Delta_N p_2} & . & e^{-i\omega\Delta_N p_M} \end{pmatrix} \begin{pmatrix} M(\omega, p_1) \\ M(\omega, p_2) \\ . \\ . \\ M(\omega, p_{NP}) \end{pmatrix} \tag{10}$$

or simply,

$$\mathbf{D}(\omega) = \mathbf{A}(\omega)\,\mathbf{M}(\omega) \tag{11}$$

The vector $\mathbf{M}(\omega)$ represents Radon solution for a monochromatic frequency component ω in a linear inverse problem. Equation 11 is usually solved using the damped least-squares method (Menke 1989; Parker 1994) that minimizes the following cost function:

$$J = ||\mathbf{D}(\omega) - \mathbf{A}(\omega)\mathbf{M}(\omega)||_2^2 + \mu||\mathbf{M}(\omega)||_2^2 \tag{12}$$

The first two terms on the right-hand side represent the data misfit, a measure of the predictive error of the forward Radon operator. The second term is a regularization (also known as damping or penalty) term to stabilize the solution. We have also introduced a trade-off parameter μ to control the fidelity to which the forward Radon operator can fit the data. The final solution is determined via minimizing Eq. 12 with respect to the unknown solution vector $\mathbf{M}(\omega)$. Once $\mathbf{M}(\omega)$ is determined for all angular frequencies ω, we can recover the Radon operator $m(\tau, p_j)$ in the time domain via inverse Fourier transform and insert the outcome into Eq. 9 for time-domain data reconstruction and interpolation. We refer to the above procedure as the damped Least-Squares Radon Transform (LSRT).

The choice of objective function in Eq. 12 is not unique. Alternatives such as non-quadratic regularization methods have been previously adopted (Sacchi and Ulrych 1995; Wilson and Guitton 2007) to increase the resolution of Radon images. For example, the regularization term can be chosen as Cauchy or L1 norm to enhance the resolution of the transform (Sacchi and Ulrych 1995). Methods based on these regularization/reweighting strategies have been referred to as High-resolution Radon Transforms (HRT). The remainder

of this review considers applications using both LSRT (for northeastern Pacific and western Canada) and HRT (for mapping global hotspots) methods.

3 *SS* Precursors and Preliminary Radon Analysis

### 3.1 Data Preparation and Problem Setup

The main data set reviewed below consists of broadband and long-period recordings from Global Seismic Network (GSN), GEOSCOPE and several regional seismic networks. We select records from shallow events (<45 km) to minimize the interference from depth phases (e.g., *sSS*); a higher cutoff value of 75 km has been adopted by global time-domain analyses (e.g., Shearer 1993; Flanagan and Shearer 1998) to improve data density at the expense of reduced data quality. We further restrict the magnitude (Mw) to >5 and epicentral distance to 100–160 deg; the latter requirement minimizes waveform interference from topside reflection *sdsS* and *ScS* precursors *ScSdScS*, where *d* denotes the depth of the corresponding reflection surface as in Fig. 1a (Schmerr and Garnero 2006). The transverse component seismograms are then filtered between 0.0013 and 0.08 Hz and subjected to a SNR (defined by the ratio between *SS* and its proceeding 'noise' level) test; all records with SNR lower than 3.0 are automatically rejected. We improve the data quality further by interactively inspecting all seismograms using a MATLAB-based visualization code and reverse the polarity of problematic station records to account for potential instrument misorientation.

We partition the data using circular, 5–10 deg (roughly equivalent to 500–1,000 km) radius spherical gathers (or "caps", Shearer 1991) of *SS* reflection points (also see Deuss, this issue). The sizes of the caps vary in order to maintain sufficient data density. The combination of natural frequency (15–20 s) and averaging radii is mainly responsible for the effective Fresnel zone of ∼1,500 km (Shearer 1993; Rost and Thomas, this issue). These mid-point gathers may partially overlap and introduce further spatial averaging within the region of interest.

3.2 Data Pre-Conditioning

In theory, LSRT/HRT can be directly applied to the reflections and conversions from mantle discontinuities. In practice, however, the recorded *SS* precursors often require additional signal enhancement due to correlated/random noise and incomplete data coverage. Without pre-conditioning LSRT/HRT cannot effectively collapse the time domain reflections to discrete $\tau-p$ values as seen in Fig. 2 since the scatter in the Radon domain can be as severe as it is in time domain (An et al. 2007). The solution is to pre-condition the time series by computing the running averages of *SS* precursors along some theoretical move-out curves. The size of the running-average (or, partial stacking) window trades off with resolution. The nominal resolution using empirical window lengths of 20–30 deg (An et al. 2007; Gu et al. 2009) is 40–50% higher than those achievable by time-domain approaches (averaged over 60–70 deg typically) within the same gather (e.g., Shearer 1993; Flanagan and Shearer 1998; Gu et al. 2003; Deuss and Woodhouse 2001; Tauzin et al. 2008). While the original time series (Fig. 5a) leads to incoherent signals in Radon space, the partially stacked series (Fig. 5b) both preserves the coherent move-outs and produces measureable Radon peaks. The superior resolution of HRT enables an effective separation of the maximum and minimum energy peaks for each seismic arrival (see Fig. 5b); only the maxima are used in the calculation of reflection depths.

Fig. 5 a Unstacked seismic traces after aligning on *SS*. The *shaded region* marks a moving-average (partial stacking) window. The averages of the *sliding windows* are plotted at the distance of the original seismograms. **b** Seismic traces after partial stacking. Weak signals corresponding to *S410S* and *S660S* are greatly enhanced
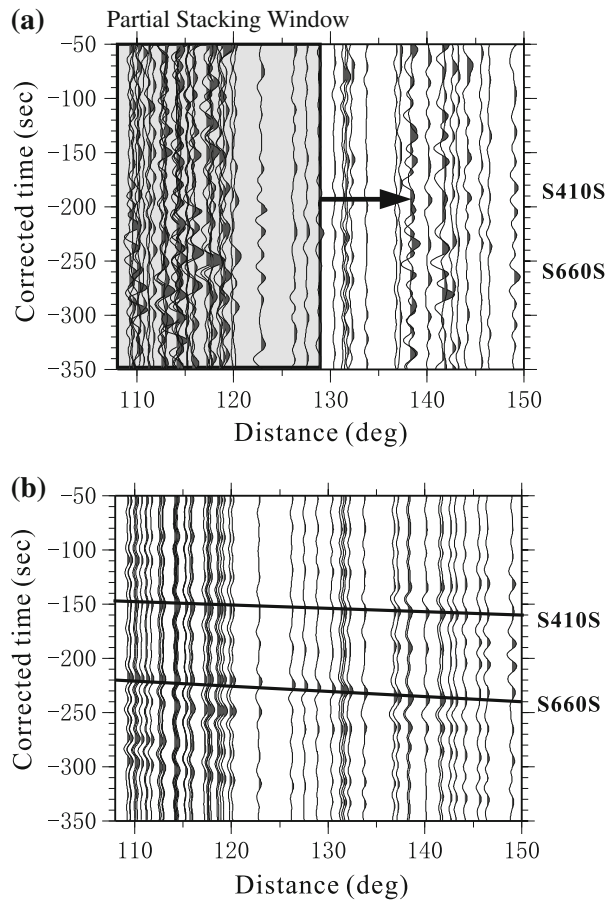
3.3 Travel Time Corrections

Travel time perturbations caused by surface topography, variable crust thickness and mantle temperature must be considered prior to Radon inversions. For the examples in this review the effects of surface topography and crust thickness at the reflection point are accounted for by ETOPO5 (distributed by National Geophysical Data Center) and CRUST2.0 (Bassin et al. 2000), respectively. We account for travel time corrections for the heterogeneous mantle using S12_WM13 (Su et al. 1994). Although the mantle temperature (or velocity) in the transition zone is a poorly constrained parameter (e.g., Romanowicz 2003; Ritsema et al. 2004), one could take small comfort in the fact that the heterogeneity corrections are in reasonable agreements among published models and do not alter the first-order observations from the LSRT and HRT imaging (Gu et al. 2009).

3.4 Radon Transform of SS Precursors

Modeling of *SS* precursor data requires source equalization and pre-conditioning. Similar to time-domain approaches, the LSRT method aligns the first major swing of the reference phase *SS* and normalize each record by its maximum amplitude. The main purpose is to

equalize the source, as the *SS-SdS* relative times are less affected by origin time uncertainty or source complexity. For consistency the ray parameter *p* of a given signal of interest (e.g., *S660S*) is expressed as the differential ray parameters to *SS*; *p* is approximately constant for the appropriate distance range (An et al. 2007; Gu et al. 2009). The process of aligning *SS* is equivalent to setting the reference ray parameter to a value of zero. Unlike time-domain analyses (see review by Deuss, this issue), Radon-based methods preserve the relative move-out between *SS* and *SdS*.

Figure 6a shows a record section of transverse-component synthetic data aligned and normalized by *SS*. The Radon model after applying HRT (Fig. 6b) recovers three well-defined energy maxima with relative *p* values of −0.10, −0.23 and −0.50 deg/s for *S220S*, *S410S* and *S660S*, respectively. Signals outside of the immediate $\tau-p$ window of interest, for instance *ScSdScS* and *sdsS/sdsS*$_{diff}$, are effectively decoupled from the reconstructed time series (Fig. 6c). Mechanisms that allow for Radon-domain windowing and post-conditioning prior to data reconstruction underscore a crucial advantage of inversion-based RT methods (e.g., LSRT and HRT) over classical RT methods. The post-conditioning criteria/algorithms are empirically determined from signal properties and tradeoff curves.

Measurement uncertainties are estimated entirely from the Radon domain. One can adopt a bootstrapping procedure (e.g., Shearer 1993) to determine τ and *p* values from random subsets of the seismic traces used in the final inversion. The standard deviation of the automatically determined Radon solutions is a reasonable estimate of the measurement uncertainty. The resulting depth uncertainty is usually less than 3 km for the measurements shown in Sect. 4.

4 Mantle Reflectivity Imaging

This section briefly reviews recent observations of the mantle reflectivity structure based on LSRT of SS precursors. Some images are modified from An et al. (2007) and Gu et al. (2009) to testify the power of LSRT and HRT in delineating the seismic reflectivity structure within the Earth's crust and mantle. We highlight the difference between advanced RT approaches and classical time- or Radon-domain approaches whenever appropriate, and refer the reader to the referenced manuscripts for in-depth discussions and interpretations of the observations. We make the following abbreviations to improve succinctness: (1) An et al. 2007 (to An07), (2) Deuss 2007 (to Deuss07), (3) Flanagan and Shearer 1998 (to FS98), (4) Upper mantle transition zone (to MTZ), and (5) 410, 520 and 660 km discontinuities (to 410, 520 and 660, respectively).

4.1 Role of Ray Parameter in Depth Estimation

A key advantage of solving for ray parameters (in addition to time) is that it provides information on the behavior (e.g., slope and continuity) of a move-out curve for a given seismic phase. This information is critical in validating the nature of the arrival. For instance, substantial deviations of measured *p* from the expected value would raise questions about the true identity of the phase, whereas relatively minor variations may be evidence of a dipping interface or a heterogeneous velocity structure. Another important contribution of the ray parameter information, which sometimes goes unnoticed, is that it improves the accuracy of the reflector depth computation. For example, previous studies (e.g., Gu et al. 1998) adopted a simple time-to-depth conversion formula based on Perturbation Theory (Dziewonski and Gilbert 1976),
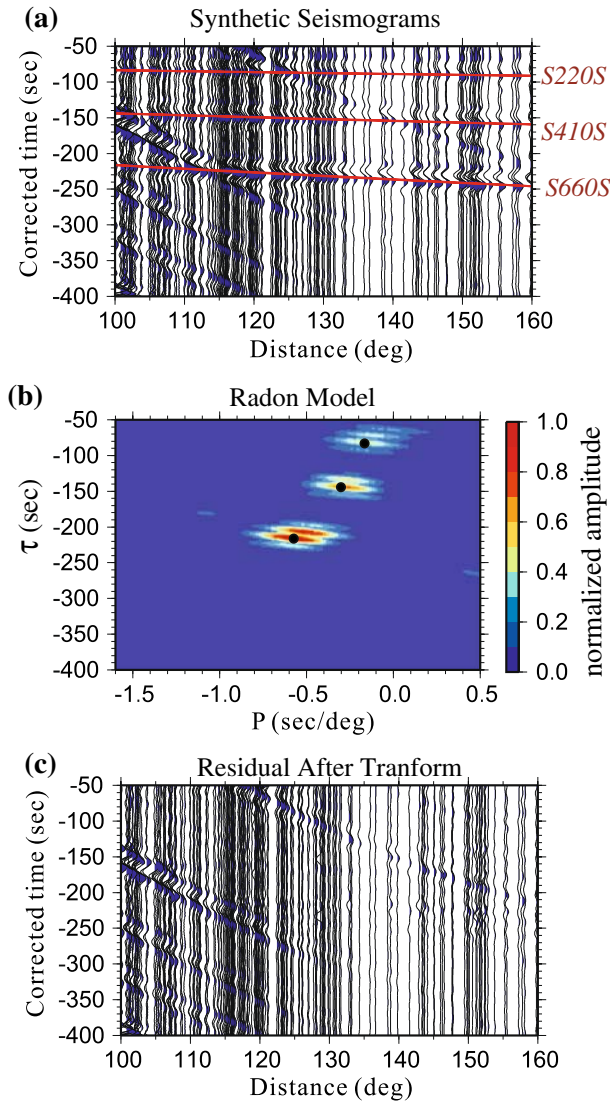
(a)   Synthetic Seismograms

(b)   Radon Model

(c)   Residual After Tranform

Fig. 6 **a** Unstacked PREM synthetic seismograms after aligning on SS. **b** Radon solution using the LSRT method. The travel–time curves of *S220S*, *S410S*, and *S660S* are mapped correctly into energetic Radon peaks. **c** Difference between the original data and predicted (or, reconstructed) time-series after Radon domain windowing. Undesired arrivals with vastly different slowness from phases of interest are effectively filtered out

$$\delta r = -\frac{\delta t \cdot r}{2}\left(\frac{r}{v(r)} - p^2\right)^{-1/2} \tag{13}$$

where r is the radius of the Earth in kilometers up to the reflector, δr is the perturbation in radius relative to PREM prediction, δt is the perturbation of reduced time, p is the measured ray parameter (not perturbation), and $v(r)$ is the shear velocity beneath the reflector.

The negative sign implies that a depressed boundary (negative δr) will cause a time delay (positive δt). This formula, as well as other approaches such as travel time ray tracing (e.g., Gossler and Kind 1996), require ray angle information to produce accurate reflector depths. However, most time-domain approaches relied on theoretical (constant) ray parameters from a reference Earth model and are, by default, less accurate than Radon-based methods (including slowness slant stacks) where dipping and heterogeneous structures are properly accounted for by the measured ray parameters.

4.2 Vespa versus LSRT

A crucial difference between slowness slant stack and inversion-based Radon methods is the latter's ability to reconstruct and interpolate time-domain data. For instance, the Radon solution and resulting misfit to the original time series can be readily adjusted through a regularization (damping) parameter (see Eq. 12). Once the desired Radon solution is obtained, one can interpolate over gaps in receiver coverage by increasing the spatial sampling of the predicted signal. Figure 7 compares the LSRT-based Radon solution with slowness slant stacks (see Eq. 2) using synthetic waveforms containing four linear events (signals). The added Gaussian noise (average to 5% the maximum amplitude) has negligible influence on the well-resolved Radon peaks (Fig. 7b). The reconstructed time series after frequency-domain re-sampling (Fig. 7c) correctly captures the event curvatures and amplitudes in the original time series. In contrast, the slowness slant stacks exhibit significant amplitude reduction and contain artifacts in and around the $\tau-p$ maxima (Fig. 7d). In the likely presence of correlated noise and waveform complexity, these seemingly negligible effects can significantly degrade the image resolution. While the image quality can be 'sharpened' by nonlinear stacking approaches (e.g., Nth-root method; Rost and Thomas 2002; Rost and Garnero 2004), the added cost of waveform distortion from these operations may be inhibitive in certain applications.

4.3 HRT versus LSRT

Under ideal data density and quality the $\tau-p$ solution for a coherent time–domain signal can be accurately determined by slowness slant stacking (e.g., Gossler and Kind 1996), LSRT (An et al. 2007) or HRT method (Gu et al. 2009). As Gu et al. (2009) demonstrated, the greatest difference among these three methods is resolution, especially in ray parameter space (Fig. 3). Owing to Cauchy-based reweighting strategy (Sacchi and Ulrych 1995; Escalante et al. 2007), the HRT method enhances the sparseness of the dominant Radon-domain signal and produces more robust, potentially more accurate, reconstructed time series than the LSRT approach (see Gu et al. 2009). The choice of regularization could influence the accuracy of time and slowness measurements when the data constraint is less than ideal. For instance, Fig. 8 compares the results of all three methods using observations beneath the Juan de Fuca hotspot (<100 traces) with non-uniform distance coverage. Apart from the obvious resolution differences, which accentuate the sparseness of the HRT solution, the relative amplitudes among the resolved Radon peaks are also influenced by the various processing strategies. For instance, both HRT and LSRT methods are able to resolve a weak (but a coherent) 520 with greater clarity than the slant-stacking (or vespa) approach. More importantly, the timing and ray parameter (relative to those of SS) for the 660 maxima differ among these three approaches (see Fig. 8). For instance, the slowness value of the HRT solution is more negative than those of the remaining approaches that, as Eq. 13 suggests, can cause considerable discrepancies in the depth of a given reflector.
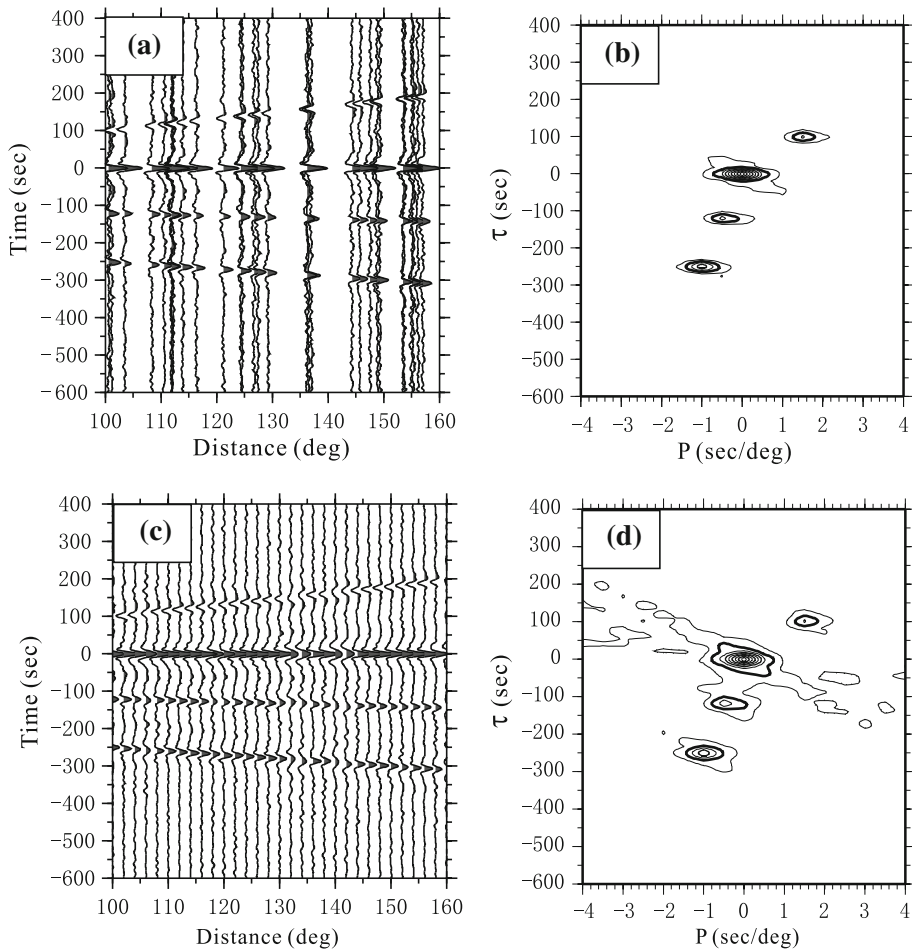
Fig. 7 a Synthetic time series with 5% (relative to *SS* maximum) Gaussian noise. **b** Resulting Radon solution based on LSRT approach. All time-domain peaks are properly mapped onto the Radon domain. **c** Interpolated and reconstructed time series based on the inverted Radon solution. **d** Resulting Radon solution obtained by the vespa process. Significant artifact is visible near the energy foci, suggesting lower image resolution

It is worth noting that while the subjective choice of smoothing parameter can have considerable influence on the 'spikiness' of the output Radon peaks, the LSRT or HRT solution for each data gather is determined empirically from the turning point of its tradeoff curve constructed from repeated inverse problems (Menke, 1989). In other words, the images shown by Fig. 8 (and those to be presented in the following sections) have been approximately 'equalized' for fair comparisons.

The section below briefly discusses recent applications of LSRT and HRT methods in mapping regional (the northeastern Pacific Ocean) and global (hypothesized 'deep hot-spot') mantle reflectivity structure. A key objective is to assess the performance of Radon inversions under diverse data constraints. Figure 9 shows the study region and the collection of SS precursors used in this part of the analysis. In the first case (Fig. 9a) the
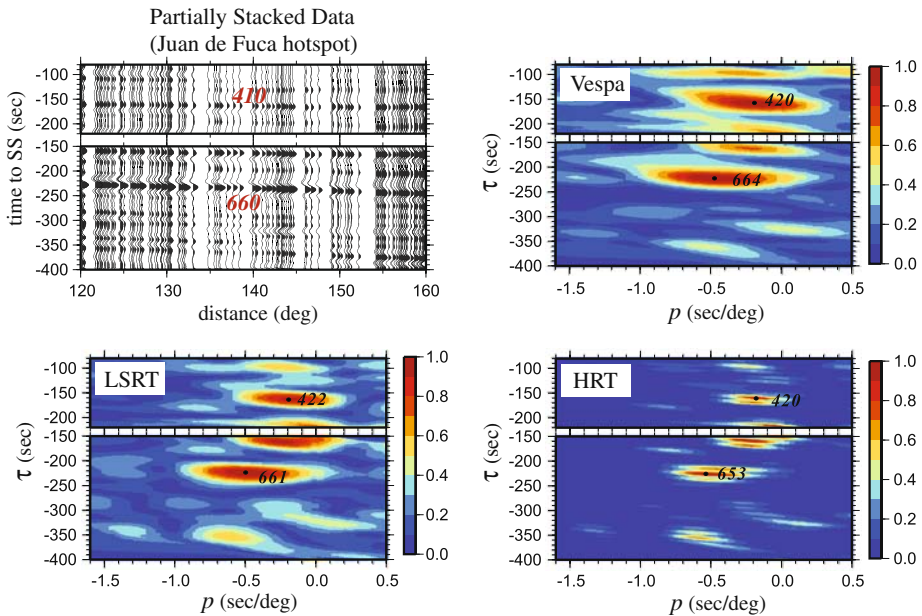
Fig. 8 Comparison of Radon transform methods using three different Radon-based methods. The original data set (not shown) has been partially stacked and the color values show the strength of the resolved Radon peaks. Apart from major improvements in signal resolution, the choice of method could affect the solution of the peaks (e.g., the depth of the 660)

density of mid-point reflections increases toward the northeast, prompting the use of variable partial-averaging windows (30 deg for the first two gathers and 20 deg for the remaining gathers) for data pre-conditioning. The global survey of hotspots utilizes a uniform cap radius of 10 deg as well as variable distance windows determined by the SNR. We restrict the distance range to 125–160 deg (instead of 100–160 deg) for some hotspots (e.g., Reunion, Hawaii among others) to remove a slowness discontinuity at a distances of $\sim$120 deg. Hotspots within the Pacific Ocean generally have greater data coverage than others.

4.4 LSRT-Based Reflectivity Imaging Beneath Northeastern Pacific Ocean and Western Canada

Partially stacked time series and Radon energy diagrams (Fig. 10) show coherent signals resulting from a series of upper mantle reflectors. The inverted τ and p values are stable for a wide range of regularization parameters (see An07), and their strengths/positions are only weakly affected by the choice of mantle velocity model. The strongest Radon energy peaks correspond to reflections from the 410 and 660, centered on τ–p values of (130–160 s, 0.2–0.4 s/deg) and (210–250 s, 0.4–0.6 s/deg), respectively. Deviations from PREM predictions directly reflect velocity and discontinuity depth perturbations from the reference 1-D mantle model. The uneven data coverage is manifested in measurement uncertainties and image resolution: for instance, extensive gaps in data distribution (e.g., Caps 1 and 2) cause the inversion problem to be under-determined and the Radon peaks to be less focused.

Fig. 9 *SS* reflection point maps
of the **a** northeaster Pacific/
western North America, and **b**
global hotspots. The averaging
radii of these two regions are
5 deg and 10 deg, respectively.
The numbers of seismograms
exceed 50 for most data gathers
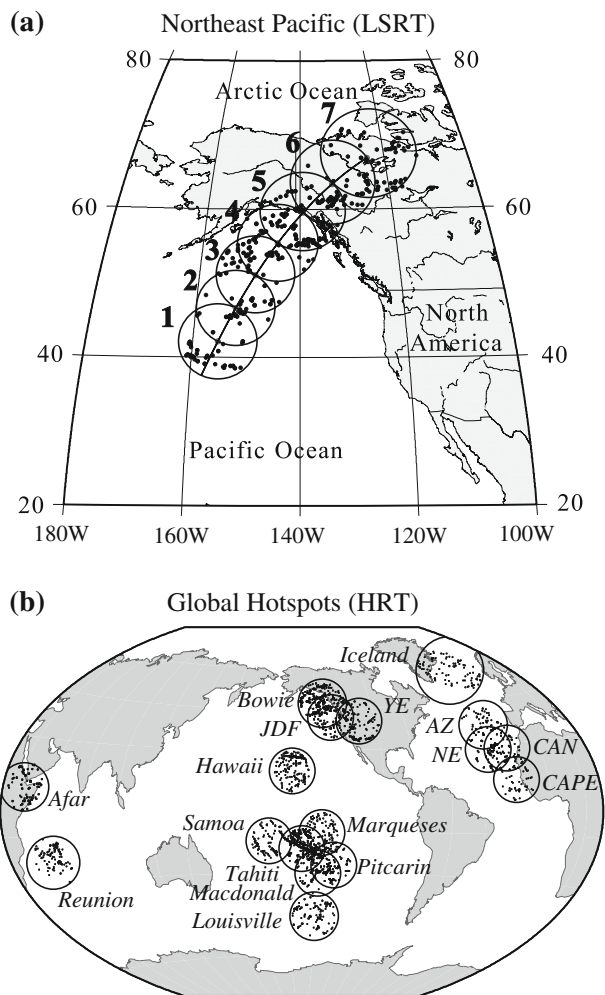
An07 converted the differential travel times between the observed and PREM-based *SS*
precursors to discontinuity depth perturbations at the intercept (see Eq. 13). Peak-to-peak
topography of ~30 km is observed on both the 410 (391–420 km) and the 660 (634–
667 km) that, despite consistent trends, far exceed the reported topography from earlier
time-domain estimates (FS98; Gu et al. 2003) along similar transects (Fig. 11a). The 410 is
raised by 20+ km relative the global average beneath the Cascadia subduction zone,
whereas the 660 shows broad, 15–20 km elevations beneath the northeastern Pacific
Ocean. These features are supported by the results of the classical RT approach based on
Eq. 2. The average depth difference between these two methods (vespa and LSRT) is
merely ~3 km (An07), which is significantly smaller than the difference between LSRT
and time-domain stacks of the same data (Fig. 11b). The larger discontinuity topography
could reflect slight improvements in lateral resolution (~1,000 km; partial stacking) by
LSRT over earlier delay-and-sum approaches (1,500+ km; stacking over the entire dis-
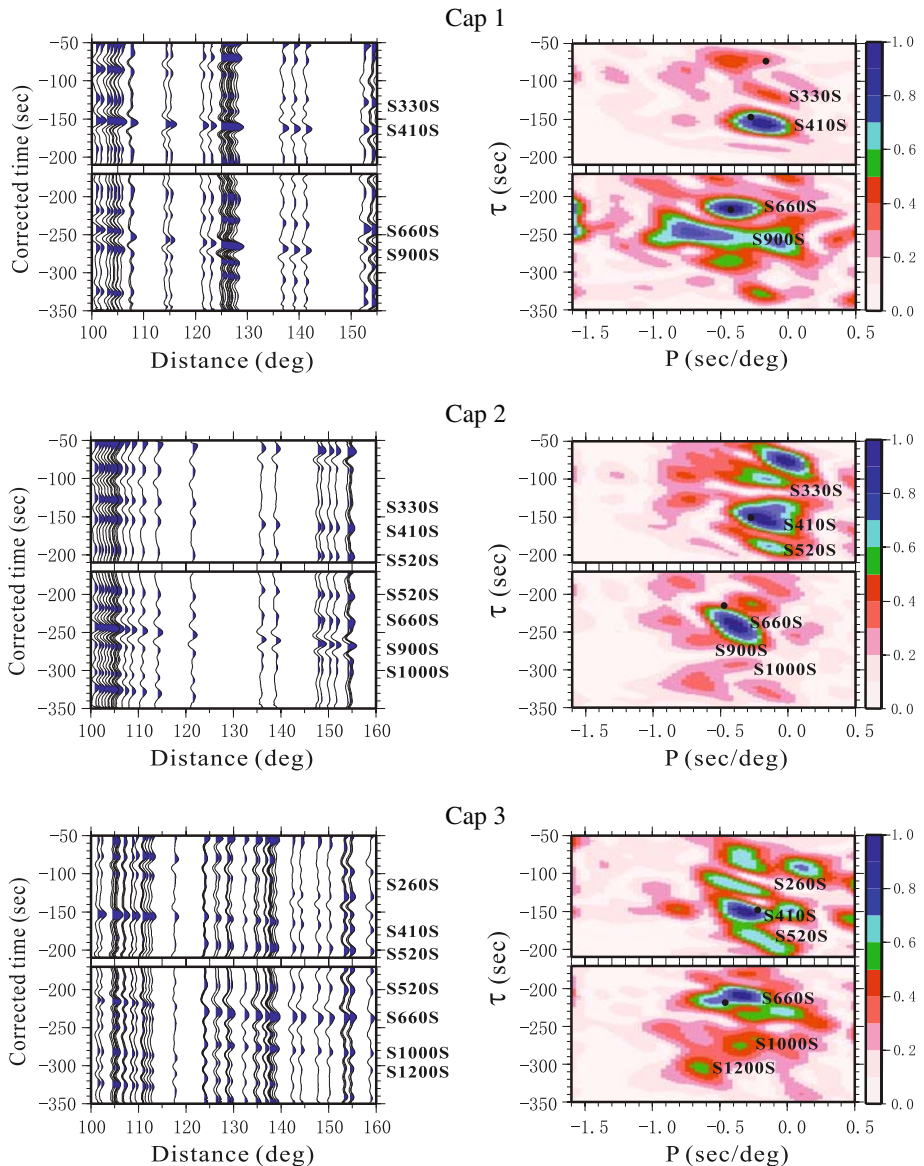tance range).

Fig. 10 Radon solutions for the southern-most three data gathers (or Caps). In each case the *left panel* shows the partially stacked data and the *right panel* shows the Radon solution after inversion. The *solid circles* denote the measured Radon peak locations from the corresponding PREM synthetic seismograms. Coherent arrivals on the time-domain traces map onto a series of energy peaks. The approximate reflection depths are as indicated by the phase names. The resolution of the Radon signals is relatively low for Caps 1 and 2 due to poorer data density and distance distribution. This figure is modified from Fig. 7 of An07

Seismic tomography lends further support for the observed topographic variations. Recent seismic reflection data (Preston et al. 2003) and converted waves (e.g., Rondenay et al. 2008) have consistently suggested the presence of old oceanic lithosphere beneath the Alaska-Cascadia subduction system at shallow mantle and, possibly, 400 km depth

Fig. 11 MTZ discontinuity depths. F & S – Flanagan and Shearer (1998). Depths obtained using LSRT are represented using Stars. *Inverted triangles* represent the results from a forward Radon (slant stack) method. *The stars* represent the results from LSRT. **a** The depth of the 410. **b** The depth of the 660. Results of these two Radon-based measurements are generally consistent, though smaller peak-to-peak topography is reported by the earlier time-domain approach (Gu et al. 2003). **c** Delay-and-sum according to the inverted ray parameter (*p*) for both synthetics (*gray*) and data (*black*). This figure is modified from the results of An07
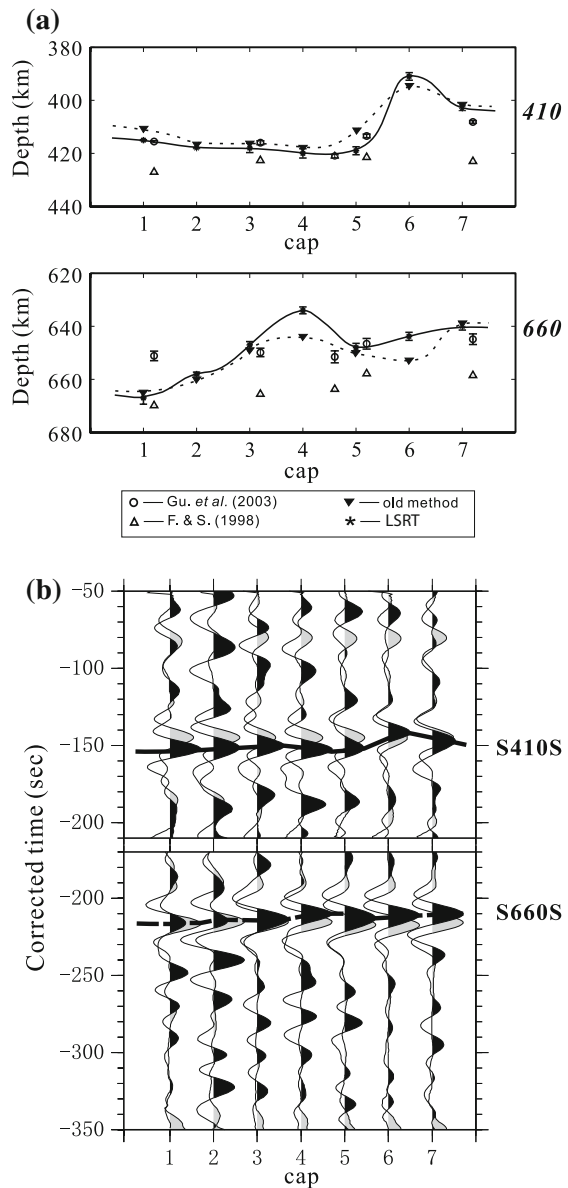
(Bostock 1996). The locations are only slightly south of Cap 6 where the shallowest part of the 410 is observed along our mid-point transect. The most notable feature on the 660, a topographic high in the northern Pacific, overlaps with a low-velocity zone within the MTZ (Fig. 11a–d). While the amplitude, depth, and dimension of the low-velocity structure differ among the selected global shear velocity models, its *existence* is uniformly suggested by velocity and by our Radon solution of the MTZ reflectivity.

Signals apart from the 410 and 660 reflections underscore the need for a Radon-based analysis. In particular, the simultaneous time and ray parameter examination is crucial to the analysis of weak, mid-MTZ reflectors due to the side-lobes of the 410 and 660

reflections (Shearer 1990, 1996; Gu et al. 1998; Deuss and Woodhouse 2001). We confidently resolve the 520 beneath the Pacific portion of the mid-point gathers, but the continental segment displays significant complexities and may imply multiple reflectors within the MTZ (Deuss and Woodhouse 2001; Fig. 11e). The depth of the 520 appears to weakly correlate with that of the 660, though the former exhibits significantly larger peak-to-peak (45 km) topography than the latter (30 km; An07). The mean depth of 545 km is slightly deeper than the reported value of 512 km based on earlier delay-and-sum analysis (FS98). Other recognizable Radon peaks are associated with mantle depths of 250, 900, 1,050, and 1,150 km (see Fig. 12e for a summary).

4.5 HRT Analysis of Global Hotspots

The case study presented in Sect. 4.4 provides a blueprint for a global mapping of mantle reflectors using RT-based imaging techniques. This section expands the scope of that pilot study by exploring the seismic reflectivity structure beneath major hotspots using HRT, a higher resolution approach based upon sparseness regularization constraints. The targets of our analysis are 17 potentially "deep-rooted" hotspots (Courtillot et al. 2003) from a recent global survey (Gu et al. 2009).

Questions regarding the genesis and depth extent of mantle plumes have persisted since the hypothesis of mantle plumes was first formulated (Morgan 1971). Proposed global catalogues based on geochemical and geophysical constraints (for reviews, see Courtillot et al. 2003; Anderson 2005; Foulger 2007) have yet to fully reconcile the wide range of surface expressions, mantle seismic wave speeds, buoyancy flux and isotopic compositions among hotspots (Courtillot et al. 2003; Steinberger et al. 2004). From a seismic perspective, observations and interpretations differ substantially even for a widely studied hotspot such as Iceland (e.g., Shen et al. 2002, 2003; Du et al. 2006). In other words, a self-consistent explanation for the origin of globally distributed hotspots requires detailed maps of both seismic velocity perturbations (e.g., Ritsema et al. 1999; Montelli et al. 2004; Zhou et al. 2006) and discontinuity structures over a larger sample size. Results from shear and compressional velocity inversions should normally be considered the first choice as mantle thermometers, unfortunately, uncertainties at MTZ depths (400–700 km) remain the Achilles' heel in the plume debate due to insufficient resolution (e.g., Romanowicz 2003; Ritsema et al. 2004). Secondary reflections and conversions offer a viable alternative in the delineation of thermal variations and impedance contrasts across mantle reflectors beneath hotspots (e.g., Li et al. 2000; Shen et al. 2003; Du et al. 2006).

For this part of the analysis we introduce averaging gathers beneath 17 potentially "deep-rooted" hotspots and seek common characteristics among them (see Fig. 9). The data density is substantially higher than that shown in Sect. 4.4 despite larger averaging areas. Sample Radon solutions of 6 hotspots (Fig. 13; see Gu et al. 2009) show a series of highly focused Radon peaks throughout the mantle above 1,400 km. The resolution of the Radon peaks is visibly higher than that presented by LSRT due to the use of sparseness constraint on the solutions. Beneath most hotspots we record a stronger reflection from the 410 than from the 660: for example, the *S410S* Radon peak is 30–50% larger than *S660S* in $\tau-p$ domain beneath the Canary and Cape Verde hotspots. The $\tau–p$ range of the two major MTZ discontinuities is slightly smaller than that detailed in Sect. 4.4, thus suggesting less peak-to-peak topography. The inferred depth of the 410 (Fig. 14a) are generally consistent with earlier results obtained by time–domain delay-and-sum (FS98; Gu et al. 2003; Lawrence and Shearer 2006; Deuss07; Houser et al. 2008), while the MTZ (Fig. 14b) is narrower than the global average of $\sim$240 km obtained using *SS* precursors (Gu et al.

(a)

(b)

S20RTS

(c) S362D1

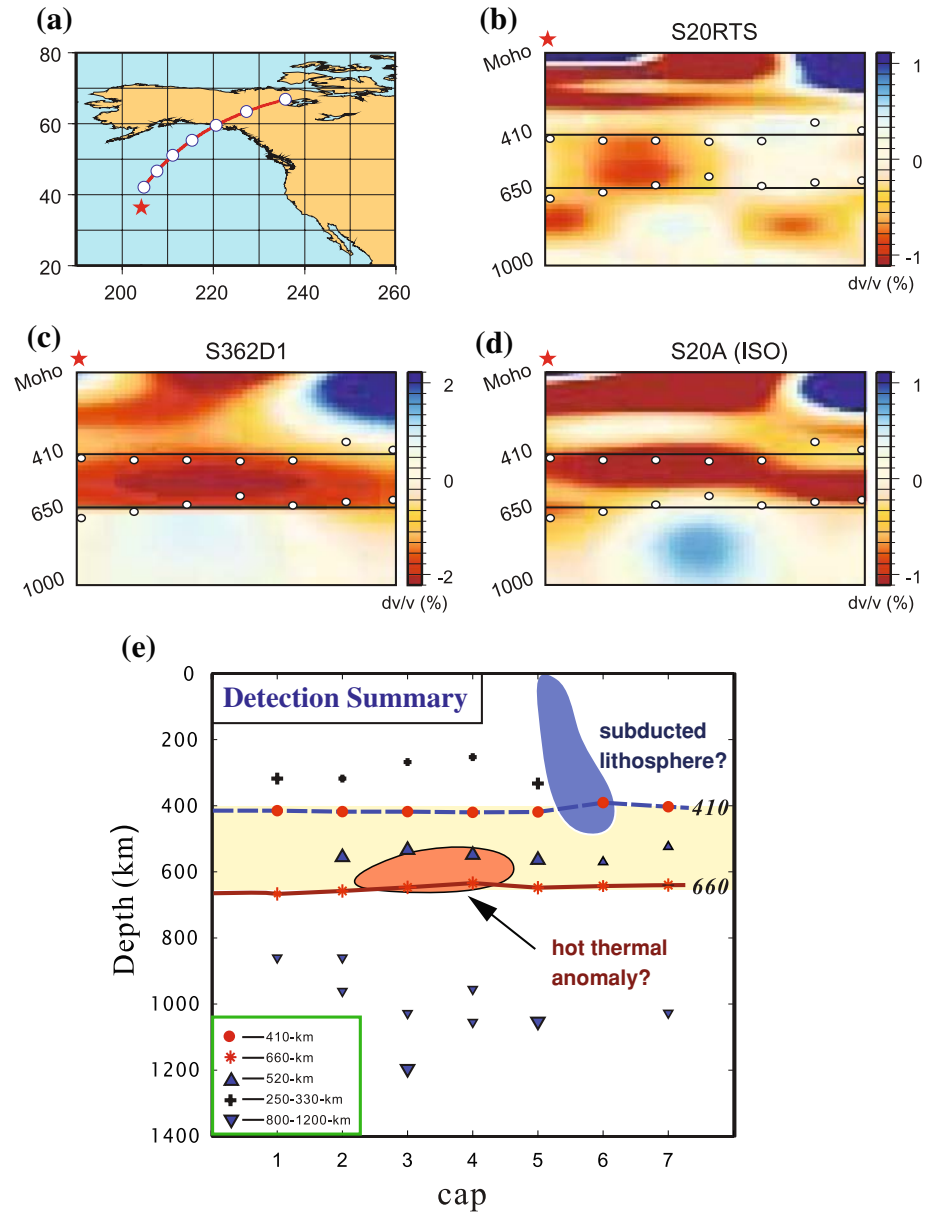**(d)** S20A (ISO)

(e)

Fig. 12 **a** Center locations of the data gathers. The three shear velocity models are **b** S362D1 (Gu et al. 2003), **c** S20A (Ekström and Dziewonski 1998), and **d** S20RTS (Ritsema et al. 1999). The *star* denotes the left-hand corner position of the cross-section. The thin MTZ beneath the northeastern Pacific Ocean overlaps with a low-velocity MTZ anomaly in the tomographic models. **e** A summary plot of the reflectivity structure beneath the data gathers. The symbol size reflects the reliability of detection. Also plotted are thermal structures that could give rise to the MTZ observations

2003; Houser et al. 2008) due to a substantially depressed 410. The latter observation is supported by a recent study of receiver functions (Lawrence and Shearer 2006), as well as by 19 out of 26 hotspots examined in Deuss07. Figure 14d summarizes the main characteristics of the MTZ beneath hotspots using a statistical comparison of several published studies. In order to differentiate the 'hotspot mantle' from the average oceanic mantle, we divide the Earth's mantle based on the tectonic regionalization scheme of Jordan (1984) and compare the median depths of the 410 under hotspots to the global and ocean averages. While the depths of the two reflectors do not appear to correlate on the global scale (Fig. 14c; Gu et al. 1998), the hotspot observations (the 410 depth, MTZ thickness) systematically differ from those pertaining to the average oceanic mantle (Fig. 14d). In particular, the median 410 depths beneath hotspots are consistently deeper than the two larger-scale averages, especially according to the two most recent studies where hotspots are carefully targeted (Deuss07) and potentially better resolved (this study). Deep 410 and thin MTZ beneath hotspots coincide with region of slow upper mantle velocities in PR5 model (Montelli et al. (2004) where the 'hotspot' mantle is, on average, 1% slower than beneath the "normal" oceanic lithosphere (see Fig. 14d).

Similar to the northeastern Pacific path, the Radon solutions also show a slew of reflections arising from the depth ranges of 200–350, 500–600, 800–920, and 1,000–1,400 km (see Fig. 13). The simultaneous τ–p constrains on these signals overcome ambiguities (Neele and de Regt 1997) that typically hamper the time-domain efforts. The HRT solution also appears sharper than the LSRT solution. The most notable signals arrive in the time range of 80–120 s prior to SS. Their timing is regionally variable, as reflections from most oceanic hotspots arrive closer to the surface reflection (SS) than hotspots near continents (e.g., the Cape Verde and Canary hotspots). These 'lithospheric' (Lehmann 1959) reflectors are notably absent in Fig. 13 beneath the northeastern Pacific Ocean. In comparison, signatures from a potential 520 are only reliably identified beneath hotspots in the northern Atlantic Ocean (e.g., Azores, Cape Verde, and Canary hotspots, mostly close to continents). The limited visibility of the 520, at $\sim$30% of the examined hotspots, is inconsistent with the earlier reports of their global (Shearer 1990) or oceanic (Gu et al. 1998; Deuss and Woodhouse 2001; see Fig. 12e) presence.

The presence of shallow lower-mantle reflectors is confirmed by seismic phases arriving 220–300 s before SS. For example, the time series from the Louisville hotpot presents multiple move-out curves that closely follow those produced by PREM. In general, the amplitude and depth of these modest reflectors are highly variable (see Fig. 12e) and their spatial distributions do not favor the oceans.

4.6 Abbreviated Interpretations and Discussions

The existence and depths of these reflectors could have significant implications for the thermal and compositional stratification(s) within the mantle (e.g., Niu and Kawakatsu 1997; Deuss and Woodhouse 2002; Shen et al. 2003; see Sect. 4.5). In comparison with time-domain approaches, the use of LSRT (Sect. 4.4) and HRT (Sect. 4.5) can lead to more accurate assessments of the existence and depth variation of known and postulated seismic reflectors. In both examples reflections from the 410 and 660 appear to be omnipresent, and their occurrences have been widely attributed to solid–solid phase transitions from α-olivine to wadsleyite (the former reflection; Katsura and Ito 1989) and from ringwoodite to magnesiowüstite ((Fe, Mg) O) and silicate perovskite ((Mg, Fe)SiO$_3$) (the latter reflection; Ringwood 1975; Ito and Takahashi 1989). Improved constraint on the depth and reflection amplitude translates to more accurate estimates of mantle temperatures in the
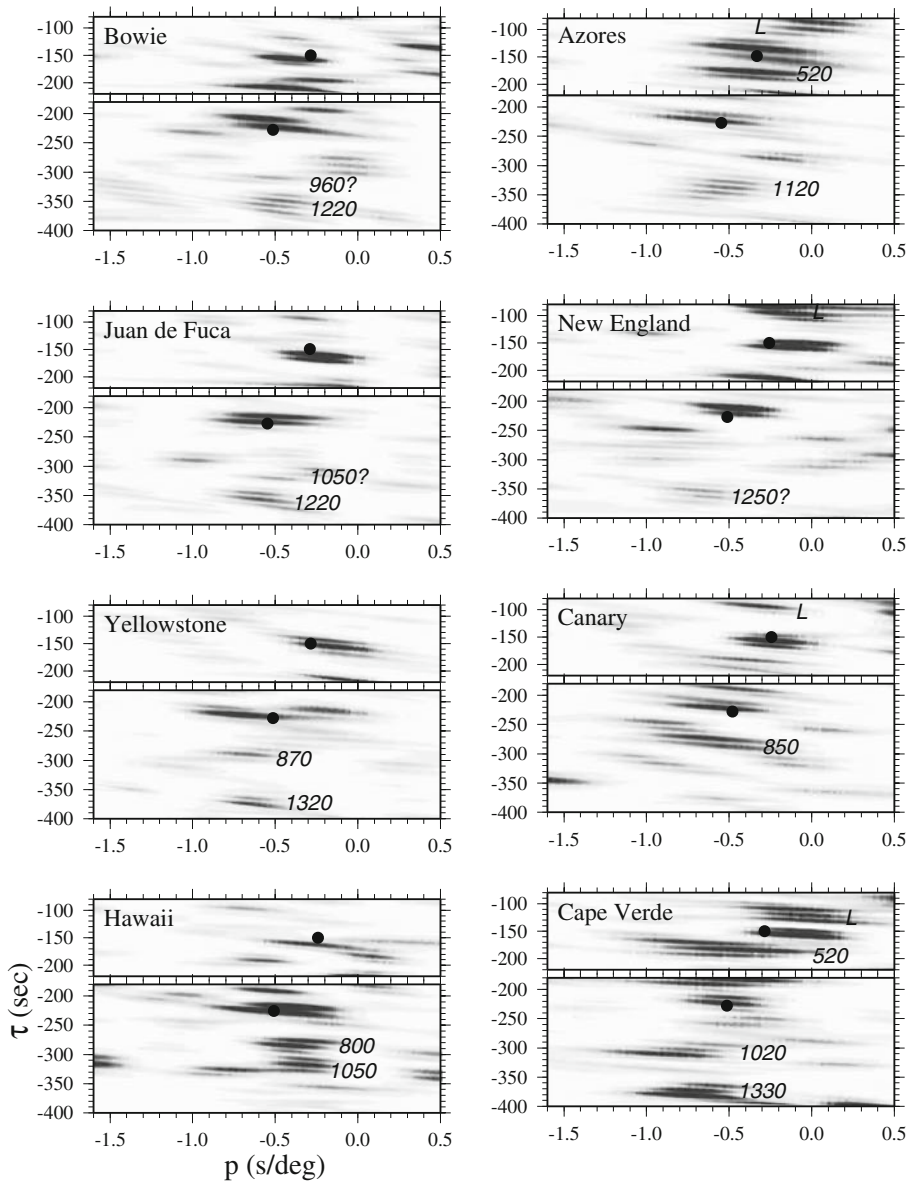
Fig. 13 Radon solutions for 8 sample hotspots. "L" represents lithospheric (Lehmann 1959) discontinuity. The *solid circles* mark the measured Radon peak locations from PREM synthetic seismograms. Apart from two robust MTZ signals, we also identify a series of reflections from other mantle depths as labeled. The 410 reflection is the most consistent signal in all but one Radon images

absence of major compositional variations. For instance, the phase boundary associated with the 410 would occur at a greater depth in a low-temperature region due to a positive Clapeyron slope (Katsura and Ito 1989; Bina and Helffrich 1994). The opposite phase boundary behavior is expected near the bottom of the upper mantle due to a negative pressure–temperature relationship (Ito and Takahashi 1989; Walker and Agee 1989).
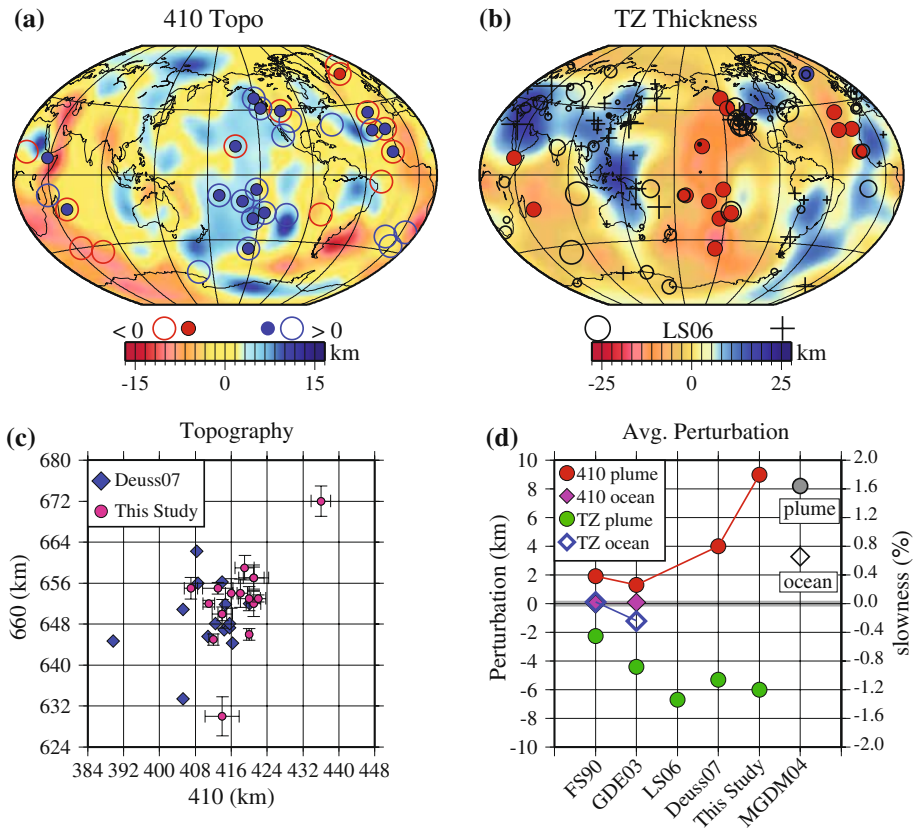
Fig. 14 **a** Depth perturbations relative to the global average of 410 km. The *background color map* shows the measurements of Gu et al. (2003). *Solid circles* represent the results of this study (only polarity is plotted against the global average) and the *large unfilled circles* show the corresponding results of Deuss07. **b** MTZ thickness perturbations relative to the global average of 242 km (based on past studies using *SS* precursors). The background color map shows the interpolated thickness measurements of Gu and Dziewonski (2002). The *foreground unfilled circles* and *crosses* represent thin and thick MTZ, respectively, from Lawrence and Shearer (2006). The *solid circles* show the results from this study. **c** Correlation (or the lack of) between the depths of 410 and 660 for both the HRT method and time-domain measurements from Deuss07. The uncertainties of our measurements are as indicated. **d** A statistical analysis of hotspot and ocean averages from various studies. In all cases the 410 is deeper and the MTZ is thinner under hotspots than oceans. The *black symbols* show the slowness (reciprocal of velocity, see right-hand axis labels) perturbations predicted by Montelli et al. (2004) shear velocity model. This plot is modified from Fig. 9 of Gu et al. (2009)

Influence of temperature on the phase boundaries offers the simplest explanation for the observed discontinuity topography beneath the northeastern Pacific Ocean and western Canada. A 30 km shallower 410 near northern British Columbia (at Cap 6; see interpretive diagram in Fig. 12) could translates to a temperature decrease of 250–350°C relative to the ambient mantle. An anomaly of such magnitude may be caused by residual subducted oceanic lithosphere both from ongoing subductions in the northwest eastern Aleutian trench and from the quartet of Kula, Farallon, Pacific and North America Plates in the past 50–55 Mya (Stock and Molnar 1988; Braunmiller and Nabelek 2002; An07). In particular, the deposition of the former Kula-Farallon plates into the mantle beneath western North America could have 'scarred' the mid-mantle (Grand et al. 1997; van der Hilst and

Karason 1999) and littered in the upper mantle (Bostock 1996; An07; Courtier and Rev-enaugh 2008). On the other hand, a hot thermal anomaly near the bottom of the upper mantle is most likely responsible for the observed elevation of the 660 in the northeastern Pacific Ocean (see Figs. 10 and 11). Although the depth of this low-velocity regime may not be sufficiently resolved by the published global shear velocity models, its existence is independently verified by the observed phase-boundary movement. Furthermore, its depth should be is closer to the bottom, rather than the top, of MTZ in order to affect the local depth of the 660. We refer the readers to An07 for in-depth discussions of the afore-mentioned topographic features.

The HRT solution of the global hotspots paints a more complex mantle picture. While the consistent depression and enhanced reflectivity of the 410 appear to be thermally driven, a relatively weak and deep 660 is inconsistent with that expected of ringwoodite to perovskite and magnesiowüstite transformation under high temperatures. Mechanisms involving water (Karato and Jung 1998; Bercovici and Karato 2003; Tonegawa et al. 2008), partial melt (e.g., Revenaugh and Sipkins 1994) and exothermic (heat-producing) majorite to Ca-perovskite transition (e.g., Weidner and Wang 1998, 2000; Hirose 2002) may be important. In fact, some of the so-called '660' on the HRT solutions could, in truth, reflect the transition of majorite garnet (rather than with the olivine) component of the MTZ (Gu et al. 2009).

Finally, LSRT and HRT methods confidently resolve a number of weak reflectors away from MTZ, with depths ranging from lithosphere to the mid mantle. Some of these reflectors (e.g., the 220, 520) are notoriously difficult to quantify due to time-domain waveform interference from stronger reflectors (e.g., surface, the 410 and 660; Deuss and Woodhouse 2002; Neele and de Regt 1997), but the aforementioned difficulty can be circumvented through signal isolation and enhancement in the transformed space. The underlying message is that reflecting structures (see Figs. 10 and 13) are fairly common beneath a wide range of tectonic regimes, including major hotspots and perceived 'quiet' oceanic regimes such as the northeastern Pacific region. Without entailing extensive details on the interpretations (see Gu et al. 2009) it suffices to say that important inferences can be made from global comparisons of reliable reflectivity images, especially images that satisfy both travel time and ray angle constraints.

5 Conclusions

This study reviews the fundamentals and simple global seismic applications of Radon transform. These methods can be equally effective on almost all short- or long-period seismic waves that are quantifiable by linear, parabolic, or hyperbolic distance–time relationships. Examples based on analysis of SS precursors show only a glimpse of the elegance and flexibility of Radon solutions. From a broader perspective, the success of Radon-based methods represents only a microcosm of contributions from many array/exploration methods currently deployed in global seismology; a number of these methods are detailed by the various contributions to this Special Issue. In short, many conceptual or practical barriers that used to divide exploration and global seismic applications are no longer withstanding. One could legitimately argue that exploration seismology is becoming a realistic, scaled-down model for global surveys. With the help of ever-improving global/regional seismic network coverage, greater successes of 'global' applications of many other high-resolution, flexible 'exploration' techniques will not be a question of *if*, but a matter of *when*.

References

An Y, Gu YJ, Sacchi M (2007) Imaging mantle discontinuities using least-squares Radon transform. J Geophys Res 112:B10303. doi:10.1029/2007JB005009

Anderson DL (2005) Scoring hot spots: the plume and plate paradigms. In: GR Foulger, JH Natland, DC Presnall, DL Anderson (eds) Plates, plumes, and paradigms, Geol. Soc. Am. Special Volume 388, 31–54

Bassin C, Laske G, Masters MG (2000) The current limits of resolution for surface wave tomography in North America. EOS Trans, AGU, 81, Fall. Meet. Suppl. F897

Bercovici D, Karato S-J (2003) Whole mantle convection and the transition-zone water filter. Nature 425:39–44

Beylkin G (1985) Imaging of discontinuities in the inverse scattering problem by inversion of a causal generalized radon transform. J Math Phys 26:99–108

Beylkin G (1987) Discrete radon transform. IEEE Trans Acoust 2:162–172 ASSP-2

Bina CR, Helffrich GR (1994) Phase transition clapeyron slopes and transition zone seismic discontinuity topography. J Geophys Res 99:15853–15860

Bostock NG (1996) Ps conversions from the upper mantle transition zone beneath the Canadian landmass. J Geophys Res 101:8393–8402

Bracewell RN (1956) Strip integration in radio astronomy. Aust J Phys 9:198–201

Braunmiller J, Nabelek J (2002) Seismotectonics of the explorer region. J Geophys Res 107:2208. doi:10.1029/2001JB000220

Chapman CH (2004) Fundamentals of seismic wave propagation. Cambridge University Press, p 632

Clayton RW, McMechan GA (1981) Inversion of refraction data by wave field continuation. Geophysics 46:860–868

Cormack AM (1963) Representation of a function by its line integrals, with some radiological applications. J Appl Phys 34:2722–2727

Courtier AM, Revenaugh J (2008) Slabs and shear wave reflectors in the midmantle. J Geophys Res 113:B08312. doi:10.1029/2007JB005261

Courtillot V, Davaillie A, Besse J, Campbell IH (2003) Three distinct types of hotspots in the Earth's mantle. Earth Planet Sci Lett 205:295–308

Davies D, Kelly EJ, Filson JR (1971) Vespa process for analysis of seismic signals. Nat Phys Sci 232:8–13

Deuss A (2007) Seismic observations of transition-zone discontinuities beneath hotspot locations. In: Foulger GR, Jurdy DM (eds) Plates, plumes and planetary processes, Geological Society Special Paper 430, 121–136, doi: 10.1130/2007.2430(07)

Deuss A, Woodhouse JH (2001) Seismic observations of splitting of the mid-transition zone discontinuity in the Earth's mantle. Science 294:354–357

Deuss A, Woodhouse JH (2002) A systematic search for mantle discontinuities using SS-precursors. Geophys Res Lett 29:1–4

Du Z, Vinnik LP, Foulger GR (2006) Evidence from P-to-S mantle converted waves for a flat "660-km" discontinuity beneath Iceland. Earth Planet Sci Lett 241:271–280

Dziewonski AM, Anderson DL (1981) Preliminary reference Earth model. Phys Earth Planet Inter 25:297–356

Dziewonski AM, Gilbert F (1976) Effect of small, aspherical perturbations on travel times and re-examination of the corrections for ellipticity. Geophys J R astr Soc 44:7–16

Escalante C, Gu YJ, Sacchi M (2007) Simultaneous iterative time-domain deconvolution to teleseismic receiver functions. Geophys J Int 171:316–325. doi:10.1111/j.1365-246x.2007.03511.x

Estabrook H, Kind R (1996) The nature of the 660-kilometer upper-mantle seismic discontinuity from precursors to the PP phase. Science 274:1179–1182

Ekström G, Dziewonski AM (1998) The unique anisotropy of the Pacific upper mantle. Nature 394:168–172

Flanagan MP, Shearer PM (1998) Global mapping of topography on transition zone velocity discontinuities by stacking SS precursors. J Geophys Res 103:2673–2692

Foulger GR (2007) The "plate" model for the genesis of melting anomalies. Geol Soc Am 430:1–28 Special Paper

Gorman A, Clowes R (1999) Wave-field tau-p analysis for 2-D velocity models: application to western North American lithosphere. Geophys Res Lett 26:2323–2326

Gossler J, Kind R (1996) Seismic evidence for very deep roots of continents. Earth Planet Sci Lett 138:1–13

Grand SP, van der Hilst RD, Widiyantoro S (1997) Global seismic tomography: a snapshot of convection in the Earth. GSA Today 7:1–7

Gu YJ, Dziewonski AM, Agee CB (1998) Global de-correlation of the topography of transition zone discontinuities. Earth Planet Sci Lett 157:57–67

Gu YJ, Dziewonski AM (2002) Global variability of transition zone thickness. J Geophys Res 107:2135. doi:10.1029/2001JB000489

Gu YJ, Dziewonski AM, Ekstrom G (2003) Simultaneous inversion for mantle shear velocity and topography of transition zone discontinuities. Geophys J Int 154:559–583

Gu YJ, Dziewonski AM, Su W-J, Ekström G (2001) Models of the mantle shear velocity and discontinuities in the pattern of lateral heterogeneities. J Geophys Res 106:11169–11199

Gu YJ, An Y, Sacchi M, Schultz R, Ritsema J (2009) Mantle reflectivity structure beneath oceanic hotspots. Geophys J Int. doi:10.1111/j.1365-246x.2009.04242.x

Hampson D (1986) Inverse velocity stacking for multiple elimination. J Can Soc Expl Geophys 22(1):44–55

Hirose K (2002) Phase transitions in pyrolitic mantle around 670-km depth: implications for upwelling of plumes from the lower mantle. J Geophys Res 107:2078. doi:10.1029/2001JB000597

Houser C, Masters G, Flanagan GM, Shearer PM (2008) Determination and analysis of long-wavelength transition zone structure using SS precursors. Geophys J Int 174:178–194. doi:10.111/j.1365-246X.2008.03719.x

Ito E, Takahashi E (1989) Postspinel transformations in the system Mg_2SiO_4–Fe_2SiO_4 and some geophysical implications. J Geophys Res 94:10637–10646

Kappus ME, Harding AJ, Orcutt J (1990) A comparison of tau-p transform methods. Geophysics 55:1202. doi:10.1190/1.1442936

Karato S-I, Jung H (1998) Water, partial melting and the origin of the seismic low velocity and high attenuation zone in the upper mantle. Earth Planet Sci Lett 157:193–207

Katsura T, Ito E (1989) The system $Mg_2S_iO_4$–$Fe_2S_iO_4$ at high pressures and temperatures; precise determination of stabilities of olivine, modified spinel, and spinel. J Geophys Res 94:15663–15670

Kawakatsu H, Watada S (2007) Seismic evidence for deep water transportation in the mantle. Science 316:1468–1471

Kruger F, Weber M, Scherbaum F, Schittenhardt J (1993) Double beam analysis of anomalies in the core-mantle boundary region. Geophys Res Lett 20:1475–1478

Lawrence JF, Shearer PM (2006) A global study of transition zone thickness using receiver functions. J Geophys Res 111:B06307. doi:10.1029/2005JB003973

Lehmann I (1959) Velocities of longitudinal waves in the upper part of the Earth's mantle. Geophys J R Astron Soc 15:93–113

Li X, Kind R, Priestley K, Sobolev SV, Tilmann F, Yuan X, Weber M (2000) Mapping the Hawaiian plume conduit with converted seismic waves. Nature 427:827–829

Ma P, Wang P, De Hoop MV, Tenorio L, Van der Hilst RD (2007) Imaging of structure at and near the core-mantle boundary using a generalized radon transform: 2. Statistical inference of singularities. J Geophys Res 112:B08303. doi:10.1029/2006JB004513

Menke W (1989) Geophysical data analysis: discrete inverse theory. Academic Press Inc., San Diego, p 289

Miller D, Oristaglio M, Beylkin G (1987) A new slant on seismic imaging: migration and integral geometry. Geophysics 52(7):943–964

Montelli R, Nolet G, Dahlen FA, Masters G, Engdah ER, Hung SH (2004) Finite-frequency tomography reveals a variety of plumes in the mantle. Science 303:338–343

Morgan WJ (1971) Convection plumes in the lower mantle. Nature 230:42–43

Neele F, de Regt H (1997) Imaging upper-mantle discontinuity topography using underside-reflection data. Geophys J Int 137(1):91–106

Niu F, Kawakatsu H (1995) Direct evidence for the undulation of the 660-km discontinuity beneath Tonga: comparison of Japan and California array data. Geophy Res Lett 22(5):531–534

Niu F, Kawakatsu H (1997) Depth variation of the mid-mantle seismic discontinuity. Geophys Res Lett 24(4):429–432

Papoulis A (1962) The Fourier integral and its applications. McGraw-Hill, New York

Parker RL (1994) Geophysical inverse theory. Princeton University Press, Princeton, p 386

Preston LA, Creager KC, Crosson RS, Brocher TM, Trehu AM(2003) Intraslab earthquakes: dehydration of the Cascadia slab. Science302(5648):1197–1200. doi:10.1126/science.1090751

Radon J (1917) Uber die Bestimmung von Funktionen durch ihre Integralverte langs gewiusser Mannigfaltigkeiten, Berichte Sachsische Academie der Wissenschaften, Leipzig. Math Phys Kl 69:262–267

Revenaugh J, Sipkin SA (1994) Seismic evidence for silicate melt atop the 410-km mantle discontinuity. Nature 369:474–476

Ringwood AE (1975) Composition and petrology of the earth's mantle. McGraw-Hill, New York, p 630

Ritsema J, Van Heijst HJ, Woodhouse JH (1999) Complex shear wav velocity structure imaged beneath Africa and Iceland. Science 286:1925–1928

Ritsema JH, van Heijst J, Woodhouse JH (2004) Global transition zone tomography. J Geophys Res 109:B02302. doi:10.1029/2003JB002610

Romanowicz B (2003) Global mantle tomography: progress status in the last 10 years. Annu Rev Geophys Space Phys 31(1):303

Rondenay S, Abers G, van Keken P (2008) Seismic imaging of subduction metamorphism. Geology 36(4):275–278. doi:10.1030/G24112A

Rost S, Garnero E (2004) A study of the uppermost inner core from PKKP and P'P' differential travel times. Geophys J Int 156:565–574. doi:10.1111/j.1365-246X.2004.02139.x

Rost S, Thomas C (2002) Array seismology: methods and applications. Reviews of Geophysics 40: 2-1–2-27. doi:10.1029/2000RG000100

Sacchi M, Ulrych TJ (1995) High-resolution velocity gathers and offset space reconstruction. Geophysics 60:1169–1177

Schmerr N, Garnero EJ (2006) Investigation of upper mantle discontinuity structure beneath the central Pacific using SS precursors. J Geophys Res 111:B08305. doi:10.1029/2005JB004197

Shearer PM (1990) Seismic imaging of upper-mantle structure with new evidence for a 520-km discontinuity. Nature 344:121–126

Shearer PM (1991) Imaging global body-wave phases by stacking long-period seismograms. J Geophys Res 96:20353–20364

Shearer PM (1993) Global mapping of upper mantle reflectors from long-period SS precursors. Geophys J Int 115:878–904

Shearer PM (1996) Transition zone velocity gradients and the 520-km discontinuity. J Geophys Res 101:3053–3066

Shearer PM (1999) Introduction to seismology. Cambridge Univ. Press, Cambridge, p 260

Shen Y et al (2002) Seismic evidence for a tilted mantle plume and north-south mantle flow beneath Iceland. Earth Planet Sci Lett 197:262–272

Shen Y, Wolfe CJ, Solomon SC (2003) Seismological evidence for a mid-mantle discontinuity beneath Hawaii and Iceland. Earth Planet Sci Lett 214:143–151

Steinberger B, Sutherland R, O'Connell RJ (2004) Prediction of emperor-Hawaii seamount locations from a revised model of global plate motion and mantle flow. Nature 430:167–173

Stock JM, Molnar P (1988) Uncertainties and implications of the Cretaceous and Tertiary position of North America relative to Farallon, Kula, and Pacific plates. Tectonics 7:1339–1384

Su WJ, Woodward RL, Dziewonski AM (1994) Degree-12 model of shear velocity heterogeneity in the mantle. J Geophys Res 99:6945–6980

Tauzin B, Debayle E, Wittlinger G (2008) The mantle transition zone as seen by global Pds phases: no clear evidence for a thin transition zone beneath hotspots. J Geophys Res 113:B08309. doi:10.1029/2007JB005364

Thorson J, Claerbout J (1985) Velocity-stack and slant-stack stochastic inversion. Geophysics 50:2727–2741

Tonegawa T, Hirahara K, Shibutani T, Takuo S, Iwamori IH, Kanamori H, Shiomi K (2008) Water flow to the mantle transition zone inferred from a receiver function image of the Pacific slab. Earth Planet Sci Lett 274:346–354. doi:10.1016/j.epsl.2008.07.046

Trad D, Ulrych TJ, Sacchi M (2002) Accurate interpolation with high-resolution time-variant Radon transforms. Geophysics 67:644–656

van der Hilst RD, Karason H (1999) Compositional heterogeneity in the bottom 1000 kilometers of Earth's mantle: toward a hybrid convection model. Science 286:1925–1928

Vidale JE, Benz HM (1992) Upper-mantle seismic discontinuities and the thermal structure of subduction zones. Nature 356:678–683

Walker D, Agee C (1989) Partitioning "equilibrium", temperature gradients, and constraints on Earth differentiation. Earth Planet Sci Lett 96:49–60

Wang P, De Hoop MV, Van der Hilst RD, Ma P, Tenorio L (2006) Imaging of structure at and near the core mantle boundary using a generalized Radon transform: 1- construction of image gathers. J Geophys Res 111, B12, B12304. doi:10.1029/2005JB004241

Wessel P, Smith WHF (1995) The generic mapping tools (GMT) version 3.0 *Technical Reference & Cookbook*, SOEST/NOAA

Wilson CK, Guitton A (2007) Teleseismic wavefield interpolation and signal extraction using high resolution linear radon transforms. Geophys J Int 168:171–181

Weidner DJ, Wang Y (1998) Chemical and Clapeyron-induced buoyancy at the 660 km discontinuity. J Geophys Res 103:7431–7441

Weidner DJ, Wang Y (2000) Phase transformations: implications for mantle structure. In: Karato S et al (eds) Earth'deep interior: mineral physics and tomography from the atomic to the global scale. Geophys. Monogr. Ser, vol 117. AGU, Washington, D. C, pp 215–235

Yilmaz O (1987) Seismic Data Processing. Soc Expl Geophys, Tulsa (Oklahoma), p 526

Zhou Y, Nolet G, Dahlen FA, Laske G (2006) Global upper-mantle structure from finite-frequency surface wave tomography. J Geophys Res 111:B04304. doi:10.1029/2005JB003677